DOI: 10.1029/2010JF001787

On the long-term memory of the Greenland Ice Sheet

I. Rogozhina,[1] Z. Martinec,[2,3] J. M. Hagedoorn,[1] M. Thomas,[1] and K. Fleming[4]

Received 31 May 2010; revised 30 November 2010; accepted 21 December 2010; published 26 February 2011.

[1] In this study, the memory of the Greenland Ice Sheet (GIS) with respect to its past states is analyzed. According to ice core reconstructions, the present-day GIS reflects former climatic conditions dating back to at least 250 thousand years before the present (kyr BP). This fact must be considered when initializing an ice sheet model. The common initialization techniques are paleoclimatic simulations driven by atmospheric forcing inferred from ice core records and steady state simulations driven by the present-day or past climatic conditions. When paleoclimatic simulations are used, the information about the past climatic conditions is partly reflected in the resulting present-day state of the GIS. However, there are several important questions that need to be clarified. First, for how long does the model remember its initial state? Second, it is generally acknowledged that, prior to 100 kyr BP, the longest Greenland ice core record (GRIP) is distorted by ice-flow irregularities. The question arises as to what extent do the uncertainties inherent in the GRIP-based forcing influence the resulting GIS? Finally, how is the modeled thermodynamic state affected by the choice of initialization technique (paleo or steady state)? To answer these questions, a series of paleoclimatic and steady state simulations is carried out. We conclude that (1) the choice of an ice-covered initial configuration shortens the initialization simulation time to 100 kyr, (2) the uncertainties in the GRIP-based forcing affect present-day modeled ice-surface topographies and temperatures only slightly, and (3) the GIS forced by present-day climatic conditions is overall warmer than that resulting from a paleoclimatic simulation.

Citation: Rogozhina, I., Z. Martinec, J. M. Hagedoorn, M. Thomas, and K. Fleming (2011), On the long-term memory of the Greenland Ice Sheet, *J. Geophys. Res.*, *116*, F01011, doi:10.1029/2010JF001787.

1. Introduction

[2] Reconstructing the history and the present-day state of the Greenland Ice Sheet (GIS) is one of the crucial keys to better understanding its possible response to global climate change. Various types of ground, airborne and spaceborne measurements are providing increasingly more useful information about the surface and bedrock topographies [e.g., *Bamber et al.*, 2001; *Layberry and Bamber*, 2001; *Letreguilly et al.*, 1991], surface velocities [e.g., *Joughin et al.*, 1997; *Thomas et al.*, 1998] and current state [e.g., *Howat et al.*, 2008; *Velicogna*, 2009] of the GIS. In addition, data obtained from boreholes, namely temperature, isotopic composition and the nature and amount of impurities, contribute to paleoclimatic reconstructions at several ice core locations [*Alley et al.*, 1993; *Dansgaard et al.*, 1993; *Etheridge et al.*, 1998; *Hammer et al.*, 1978, 1985; *Jouzel et al.*, 1993, 1997; *Meese et al.*, 1994; *Petit et al.*, 1999; *Sowers et al.*, 1993; *Watanabe et al.*, 2003]. Dynamic and thermodynamic states of the entire ice sheet can, however, only be described by ice sheet models.

[3] Due to the long-term thermomechanical response of the polar ice sheets, the evolutionary processes are slow in comparison to the temporal and spatial variability of the climatic states of the surrounding atmosphere and ocean. For example, *Calov and Hutter* [1996] demonstrated that the present-day temperature distribution within the GIS is even affected by the conditions during the penultimate glacial cycle. This fact underlines the importance of an appropriate spin-up or initialization of an ice sheet model to obtain accurate estimates of the present-day velocity-temperature distribution of ice sheets.

[4] A number of studies dealing with the past, present and future states of the Earth's ice sheets have been conducted using three-dimensional thermomechanical ice sheet models. The most common techniques employed to initialize the present-day and past states (surface elevation, temperature and velocity fields) of an ice sheet model are (1) transient simulations driven by paleoclimatic temperature reconstruction [*Charbit et al.*, 2007; *Greve*, 1997b; *Greve et al.*, 1998, 1999a; *Huybrechts and de Wolde*, 1999; *Johnson and Fastook*, 2002; *Le Meur and Huybrechts*, 2001; *Pattyn*, 1999; *Ridley et al.*, 2005; *Tarasov and Peltier*, 1999, 2003; *van de Wal*, 1999] and (2) steady state simulations driven by the present-day or past climatic conditions [*Baldwin et al.*, 2003; *Calov and*

[1]Helmholtz Centre Potsdam, GFZ German Research Centre for Geosciences, Section 1.3: Earth System Modelling, Potsdam, Germany.
[2]Dublin Institute for Advanced Studies, Dublin, Ireland.
[3]Department of Geophysics, Faculty of Mathematics and Physics, Charles University, Prague, Czech Republic.
[4]Western Australian Centre for Geodesy, Curtin University of Technology, Perth, Western Australia, Australia.

0148-0227/11/2010JF001787

Hutter, 1996; *Greve*, 1997b; *Huybrechts*, 1996; *Huybrechts and T'siobbel*, 1995; *Kubatzki et al.*, 2006; *Pattyn*, 2006; *Payne and Baldwin*, 1999; *Rybak and Huybrechts*, 2008; *Takeda et al.*, 2002; *Zweck and Huybrechts*, 2003]. Both procedures are equally popular, although in more recent studies, there is a tendency to compute the present-day and past states of ice sheet models by paleoclimatic rather than steady state simulations.

[5] The lack of information about Greenland's past ice cover implies that transient simulations of ice sheet models driven by paleoclimatic records are often started from either (1) present-day topographies with artificially prescribed temperatures and ages of the ice [*Greve* 1997c, 2000; *Huybrechts*, 2002; *Huybrechts et al.*, 2007], (2) relaxed lithosphere without ice load [*Budd et al.*, 1998; *Greve et al.*, 1999b], (3) the results of spin-up transient simulations driven by artificially prolonged paleoclimatic records [*Abe-Ouchi et al.*, 2007; *Calov and Hutter*, 1996; *Ritz et al.*, 2001], or (4) the results of steady state simulations under present-day or past climatic conditions [*Calov et al.*, 2005a, 2005b; *Marshall and Cuffey*, 2000; *Pattyn and Decleir*, 1998; *Tarasov and Peltier*, 2002].

[6] The usual procedure is to spin up an ice sheet model over one or two glacial cycles [e.g., *Abe-Ouchi et al.*, 2007; *Calov*, 2006; *Greve*, 1997c; *Huybrechts*, 1994, 1996]. Although the longest Greenland ice core record dates back to 250 kyr BP [*Dansgaard et al.*, 1993], it is generally acknowledged that prior to 105 kyr BP (or even 100 kyr BP) it is distorted by ice-flow irregularities [*Andersen et al.*, 2004]. Therefore, none of the currently available Greenland ice core records can provide reliable data about climatic variations within one or two glacial-interglacial cycles.

[7] This paper aims to analyze the effects of various initial conditions, simulation times and climatic forcing on the present-day and former states of a model of the GIS. We first introduce the ice model SICOPOLIS [*Greve*, 1995] and the climate forcing. Next we discuss the results, which arise from a number of simulations where parameters such as the timescale of the simulations, the actual climatic forcing and the start-up conditions are tested. Our findings are summarized in section 4.

2. Methodology

2.1. Ice Sheet Model

[8] In this study, we use the polythermal ice sheet model SICOPOLIS [*Greve*, 1997a], which is based on the shallow ice approximation (SIA) [*Hutter*, 1982, 1983; *Morland*, 1984] and the rheology of an incompressible, heat conducting, power law fluid [see *Hutter*, 1983; *Paterson*, 1994]. It simulates the time-dependent extent, thickness, 3-D velocity and temperature distributions, water content and age of grounded ice in response to external forcing. When employing the SIA, the flow velocity is proportional to surface gradient, which typically tends toward infinity as an ice sheet's margin is approached [*Greve*, 1995]. As a consequence, large thickness errors at the margins of a modeled ice sheet influence modeled present-day calving and melting rates [*Bueler et al.*, 2005], and thereby short-term present-day and future predictions. The present-day GIS resulting from paleoclimatic simulations computed by a SIA-based model can nonetheless still be used to estimate general trends in the future evolution of the GIS under various climatic conditions [*Greve*, 2000; *Ridley et al.*, 2005]. Furthermore, for accurate short-term predictions, more sophisticated approaches must be applied (for example, assimilation techniques, as by *Arthern and Hindmarsh* [2006] and *Arthern and Gudmundsson* [2010], and more complex models of ice dynamics, as discussed by *Rückamp et al.* [2010]). However, an accurate reconstruction of the margins of the present-day GIS is beyond the scope of this paper, which aims at analyzing the large-scale time-space characteristics of the GIS.

[9] In this study, all simulations are undertaken following the conventional cold-ice method (see Appendix A for the model equations). The temperature equation for the cold-ice regions is solved for the entire ice sheet, while the basal temperatures above pressure melting point are artificially reset to the pressure melting point. The thermomechanical coupling is described by the temperature-dependent rate factor [*Greve et al.*, 1998]. The isostatic adjustment of the lithosphere to the changing ice load is modeled by the local lithosphere–relaxing asthenosphere approach with an isostatic time lag $\tau_\nu = 3$ kyr (for more details, see *Greve* [2001] and *Le Meur and Huybrechts* [1996]). For the steady state simulations, the computation of the lithosphere temperature, governed by equation (A5), is switched off and the geothermal heat flux is imposed directly at the ice base since the thermal inertia of the lithosphere is only important during the ice sheet's evolution under conditions of temporally varying surface temperature, hence it does not influence the results of steady state runs.

[10] External forcing entering the boundary conditions is specified by (1) mean annual air temperature and amplitudes of the seasonal temperature changes, (2) surface mass balance, namely, precipitation and ablation, (3) global sea level, and (4) geothermal heat flux. Surface melting is parameterized by the degree-day method [*Reeh*, 1991] and the semi-analytical solution for the positive-degree day integral [*Calov and Greve*, 2005]. The degree factors are identical to those used by *Greve* [2005].

2.2. Climate Forcing and Simulation Setup

[11] The components of climate forcing are taken to be identical to those used by *Greve* [2005], with the exception of various time-dependent factors describing air temperature variations over time, termed the glacial index $g(t)$. These values are based on the GRIP and combined Vostok-GRIP [*Greve*, 2005] ice core records reaching back to 250 and 400 kyr BP, respectively [*Dansgaard et al.*, 1993; *Petit et al.*, 1999]. Both time series have a Gaussian filter with 2 kyr filter width applied to them for the period prior to 100 kyr BP [*Greve*, 2005]. Following *Charbit et al.* [2002, 2007], *Forsström et al.* [2003], *Forsström and Greve* [2004], *Greve* [2005] and *Tarasov and Peltier* [2004], climate forcing is constructed based on the present-day and Last Glacial Maximum (LGM) distributions of precipitation/accumulation and surface temperature. The LGM anomaly fields are provided by the atmospheric general circulation model UKMO [*Hewitt and Mitchell*, 1997] and corrected for temperature changes due to varying ice-surface elevation by *Greve* [2005]. The glacial index $g(t)$ is employed to scale precipitation and surface-temperature fields between the present-day and LGM climatic conditions (see Appendix B). It is defined such that $g(t) = 1$ denotes LGM conditions, while $g(t) = 0$ corresponds to the present-day climatic conditions.

Table 1. Description of the Naming Scheme Followed and the Parameters Used in the Transient and Steady State Runs Carried Out in This Study[a]

Run Name	Initial Conditions	Run Time	Source of Forcing	Section
IC_250_VG	Ice-covered bedrock	250 kyr	Vostok (250 to 100 kyr BP) and GRIP (100 kyr BP until today)	3.1, 3.3
IF_250_VG	Ice-free relaxed lithosphere	250 kyr	Vostok (250 to 100 kyr BP) and GRIP (100 kyr BP until today)	3.1, 3.2
IC_400_VG	Ice-covered bedrock	400 kyr	Vostok (400 to 100 kyr BP) and GRIP (100 kyr BP until today)	3.1, 3.2
IF_400_VG	Ice-free relaxed lithosphere	400 kyr	Vostok (400 to 100 kyr BP) and GRIP (100 kyr BP until today)	3.1, 3.2
IF_240_VG	Ice-free relaxed lithosphere	240 kyr	Vostok (240 to 100 kyr BP) and GRIP (100 kyr BP until today)	3.2
IF_238_VG	Ice-free relaxed lithosphere	238 kyr	Vostok (238 to 100 kyr BP) and GRIP (100 kyr BP until today)	3.2
IC_250_G	Ice-covered bedrock	250 kyr	GRIP (250 kyr BP until today)	3.3
IC_150_SS_100_G	Ice-covered bedrock	150 + 100 kyr	Steady state (SS) forcing with constant $g(t)$ = 0.184 corresponding to the climatic conditions at 100 kyr BP (150 kyr) GRIP (100 kyr BP until today)	3.3
IC_100_G	Ice-covered bedrock	100 kyr	GRIP (100 kyr BP until today)	3.3
IC_250_SS	Ice-covered bedrock	250 kyr	Steady state (SS) forcing with constant $g(t)$ = 0 corresponding to the present-day climatic conditions	3.3

[a]IC means initially ice covered, IF is initially ice free, SS is steady state, V is Vostok, and G is GRIP, and the numbers indicate the simulation time in thousands of years (kyr). The ice-covered simulations start with present-day ice-surface and bedrock topographies using artificially prescribed temperatures and ages of the ice inside the ice body (as discussed in section 3.1); the ice-free runs are started from the ice-free relaxed lithosphere.

[12] The steady state simulations are computed using a constant glacial index, and the spatial distribution of the atmospheric forcing fields which are determined according to equations (B1)–(B3). In this study, we assume that a steady state is reached when all of the fundamental quantities such as ice volume, ice-covered area, mean temperature and mean velocity (see section 3.3, equations (1) and (2)) have remained unchanged (or their variations have not exceeded 0.05%) over the course of at least 10 kyr.

[13] The spatially variable geothermal heat flux is based on *Pollack et al.* [1993] as modified by *Greve* [2005] in order to achieve a better agreement between measured and modeled basal temperatures in the areas of the four deep ice cores. The sea level forcing z_{sl}, which determines the land area available for glaciation, is derived from the SPECMAP marine δ^{18}O record [*Imbrie et al.*, 1984] as described by *Greve* [2005]. The horizontal grid spacing is 20 km by 20 km, corresponding to 82 by 140 grid points in the stereographic plane. In the vertical direction for the cold ice layers, the σ transformation is used such that 81 grid points are remapped to [0, 1] intervals. The bedrock is described by 11 equidistant grid points. Using the standard settings of the SICOPOLIS model, in both transient and steady state simulations, the enhancement factor E is coupled to the age of the ice A (see Appendix C, equations (C1) and (C2)). The nomenclature of the naming scheme followed in the simulations, their initial states, simulation time intervals, and their order of appearance in this paper are summarized in Table 1.

3. Results and Discussion

3.1. Initial Configuration and Simulation Time

[14] We now present the results of the first series of four paleoclimatic simulations of the GIS driven by the surface-temperature history inferred from the GRIP and Vostok ice core records. Following *Greve* [2005], all runs are driven by glacial index values based on a combination of these two ice core records (Figure 1a). Run IC_250_VG is started from 250 kyr BP with the present-day surface and bedrock topographies [*Bamber et al.*, 2001; *Layberry and Bamber*, 2001] as the initial state (ice-covered initial condition). The temperature of the ice body is uniformly set equal to –10°C and the initial age of the ice is up to 15 kyr [*Greve*, 1997b]. Run IF_250_VG also starts from 250 kyr BP, but from the ice-free relaxed lithosphere state (ice-free initial condition). Both simulations are run until the present day. Therefore, apart from the difference in the initial ice sheet topographies, runs IC_250_VG and IF_250_VG are identical. In addition, we carry out two longer runs, IC_400_VG and IF_400_VG, with a simulation period from 400 kyr BP until the present and again with initial ice-covered (IC) or ice-free (IF) conditions, respectively (see Table 1 for a description of the nomenclature used in naming the runs).

[15] Since the basal layers of an ice sheet consist of old ice, and can, thus, be considered as a depository of the ice sheet's long-term memory, we pay particular attention to the temperatures of the basal ice layers. Mean basal (MB) temperature is computed in this study as the mean temperature of a 150 m thick basal layer averaged over the area of the GIS where ice thickness exceeds 1.5 km. Similarly, we define the Summit mean basal (SMB) temperature as the mean temperature of a 150 m thick basal layer averaged over an area of 6400 km^2 (approximately 0.35% of the total area covered by the present-day GIS) surrounding the Summit of the GIS (the location of the GRIP station), since in this area the longest ice cores were recovered from the GIS (GRIP as used in this work, and GISP2 [*Mayewski and Bender*, 1995]). In the simulations with ice-free start-up conditions, MB and SMB temperatures are calculated starting from the moment when the thickness of the ice sheet reaches 1.5 km for at least one grid point. However, this criterion results in irregularities in the temperature evolution at the beginning of the ice-free simulations until the area of 1.5 km thick ice is sufficiently large for averaging.

[16] The volumes and basal temperatures of the simulated GIS are presented in Figure 1. Even after 250 kyr of simulation, the resulting ice volumes obtained by runs IC_250_VG (black curve) and IF_250_VG (blue curve) still differ by about 4% (Figure 1b). For the runs IC_400_VG and IF_400_VG, the present-day volumes are very nearly the same, with only 0.85% difference. The differences in the present-day MB temperatures (Figure 1c) and SMB temperatures (Figure 1d) between the IC_250_VG and IF_250_VG runs are 1.4°C and 4.1°C, respectively. On the other hand, the longer runs,

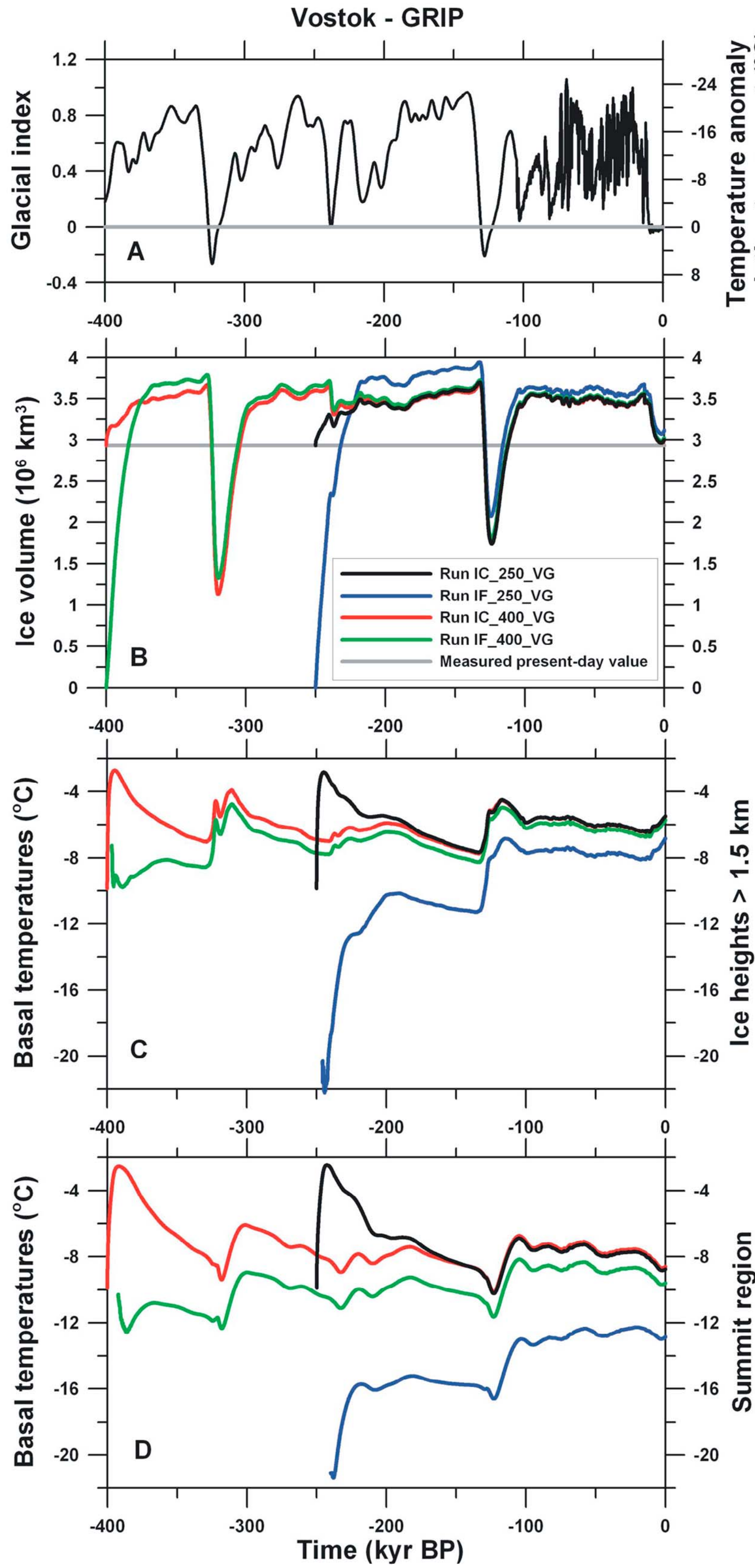

Figure 1. (a) Time-dependent component of atmospheric forcing: glacial index based on a combination of the GRIP and Vostok records [*Greve*, 2005]. (b) Volume changes in the modeled GIS in response to climate variations (transient runs IC_250_VG, IF_250_VG, IC_400_VG, and IF_400_VG; see Table 1). (c) MB temperatures. (d) SMB temperatures.

IC_400_VG and IF_400_VG, show MB temperature variations in very good agreement with each other, although the present-day SMB temperatures differ by 1°C due to the effect discussed in section 3.2. Both longer runs reveal MB and SMB temperature variations of the order of 3–4°C during the last two glacial-interglacial cycles, meaning the above mentioned differences between present-day values are a substantial proportion of the expected variability. Both the volume and basal temperature values obtained by run IC_250_VG converge to the corresponding values for these quantities determined by run IC_400_VG relatively quickly. For example, after 100 kyr of simulation, there is already hardly any difference in their respective volumes or basal temperatures.

[17] In Figure 2, the differences in the ice sheet topographies simulated by the four runs are shown. Figures 2a and 2c illustrate how runs IC_250_VG (Figure 2a) and IC_400_VG (Figure 2c, plotted as the difference in the final topographies between runs IC_400_VG and IC_250_VG) arrived at similar present-day ice-surface topographies where the differences between ice sheets are less than 10 m for much of their extent. We may therefore conclude that a longer simulation IC_400_VG is not necessarily needed to reach a realistic description of the present-day ice sheet. However, there are local differences of the order of 100–200 m at the margins of the modeled ice sheets resulting from runs IC_250_VG and IC_400_VG. A major reason for this is the use of the SIA, which, as discussed in section 2.1, results in significant errors in the estimates of flow velocities in the vicinity of ice sheet margins.

[18] The comparison of the final ice-surface topographies obtained by runs IC_250_VG and IF_400_VG (Figure 2d) does not reveal substantial differences between them (generally less than 20–30 m), while the difference between runs IF_250_VG and IC_250_VG (Figure 2b) shows a larger area covered by more noticeable differences in topographies (up to 50 m). The values of the discrepancies shown in Figures 2b and 2d are overall positive, whereas the values in Figure 2c are mostly negative, meaning that both ice sheets resulting from the initially ice-free runs are thicker than those computed by the initially ice-covered simulations. This can be explained by lower basal temperatures and, consequently, lower basal melting rates, resulting from the initially ice-free simulations (see section 3.2).

[19] The long transient simulation carried out by run IC_400_VG results in the best fit between the observed (2.93×10^6 km^3) and modeled (2.998×10^6 km^3) present-day ice volumes among all other runs. Runs IC_250_VG, IF_250_VG and IF_400_VG produce larger ice volumes of 3.002×10^6 km^3, 3.113×10^6 km^3 and 3.024×10^6 km^3, respectively. We can see a good fit between both the present-day temperatures (Figure 1) and topographies (Figure 2) computed by three runs, IC_250_VG, IC_400_VG and IF_400_VG, indicating that the final states of these simulations are not crucially affected by the differences in the initial conditions or simulation times. On the other hand, the differences in the present-day topographies computed by runs IC_250_VG and IF_250_VG exceed 50 m over most of the ice sheet's surface and reach values of 100–150 m in the north (5–15% of the total ice thicknesses) and in the Summit region (more than 3% of the ice thicknesses) of the modeled GIS. The simulations discussed in section 3.3 confirm that the northern and central areas of the GIS are most affected by the memory of the different initial states.

3.2. Ice-Free Start-Up Conditions and Initial Climate

[20] In this section, we study the influence of the initial surface temperatures on the thermodynamic state of the GIS as described by transient runs with ice-free initial conditions. Runs IF_250_VG and IF_400_VG (section 3.1) differ not only by the length of their simulation times, but also by the initial surface temperatures. This is defined by the values of glacial index to be 0.734 and 0.179 at 250 kyr BP and 400 kyr BP, respectively (see Figure 1a), which means that the initial surface temperature employed in IF_250_VG for the Summit area (specifically, at the location of the GRIP station) is approximately 13°C lower than the equivalent in run IF_400_VG.

[21] Due to both geothermal heat flux and dissipative strain heating, the basal temperatures are significantly higher than the ice-surface temperatures. Present-day measurements reveal a difference of more than 20°C between the temperatures of the uppermost and basal layers in the Summit region [*Cuffey et al.*, 1995; *Johnsen et al.*, 1995]. In addition, as shown in section 3.1, basal temperature variations in the areas of thicker ice are around 3–4°C over the course of the last two glacial-interglacial cycles, while average surface temperatures may differ by more than 20°C within a glacial-interglacial period. Following the common assumption that the GIS is about 3 million years old, we may conclude that 400 kyr and 250 kyr ago, the basal layers of the GIS were significantly warmer than the uppermost layers. By contrast, at the initial stage of simulations with ice-free start-up conditions (at 400 kyr or 250 kyr BP), a thin ice layer is formed from snowfall, which has the same temperature as the snow that is accumulating over the land surface.

[22] For the case of an ice-free column, the numerical code SICOPOLIS solves the temperature equation for the bedrock (see equation (A5)) by applying the air temperature as a boundary condition at the surface of the lithosphere. Thus, the signal of the initial climatic conditions leaks into the bedrock. If the initial climate is glacial, the temperatures of the basal layers and underlying bedrock modeled by a transient simulation are extremely cold as opposed to the realistic thermodynamic state of an existing ice sheet. However, if interglacial climate is taken as the initial state, the adjustment of both the newly formed basal layers and the bedrock is much faster.

[23] To demonstrate this effect, we carry out two runs to assess the effect of initial glacial or interglacial temperature conditions (see Figure 3). Runs IF_240_VG (orange curves) and IF_238_VG (green curves) are identical to run IF_250_VG except for the durations of simulations, which are equal to 240 kyr and 238 kyr, respectively, and as a result, also have different initial values of the glacial index, which are equal to 0.227 and 0, respectively. Both values describe interglacial climatic conditions, whereas the initial climate for run IF_250_VG (blue curves) is glacial with a glacial index $g(t_0) = 0.734$. The initial air temperatures for run IF_238_VG therefore correspond to the hypothetical present-day temperatures over the ice-free Greenland area (see the parameterization by *Ritz et al.* [1997]). For runs IF_250_VG and IF_240_VG, the respective initial air tem-

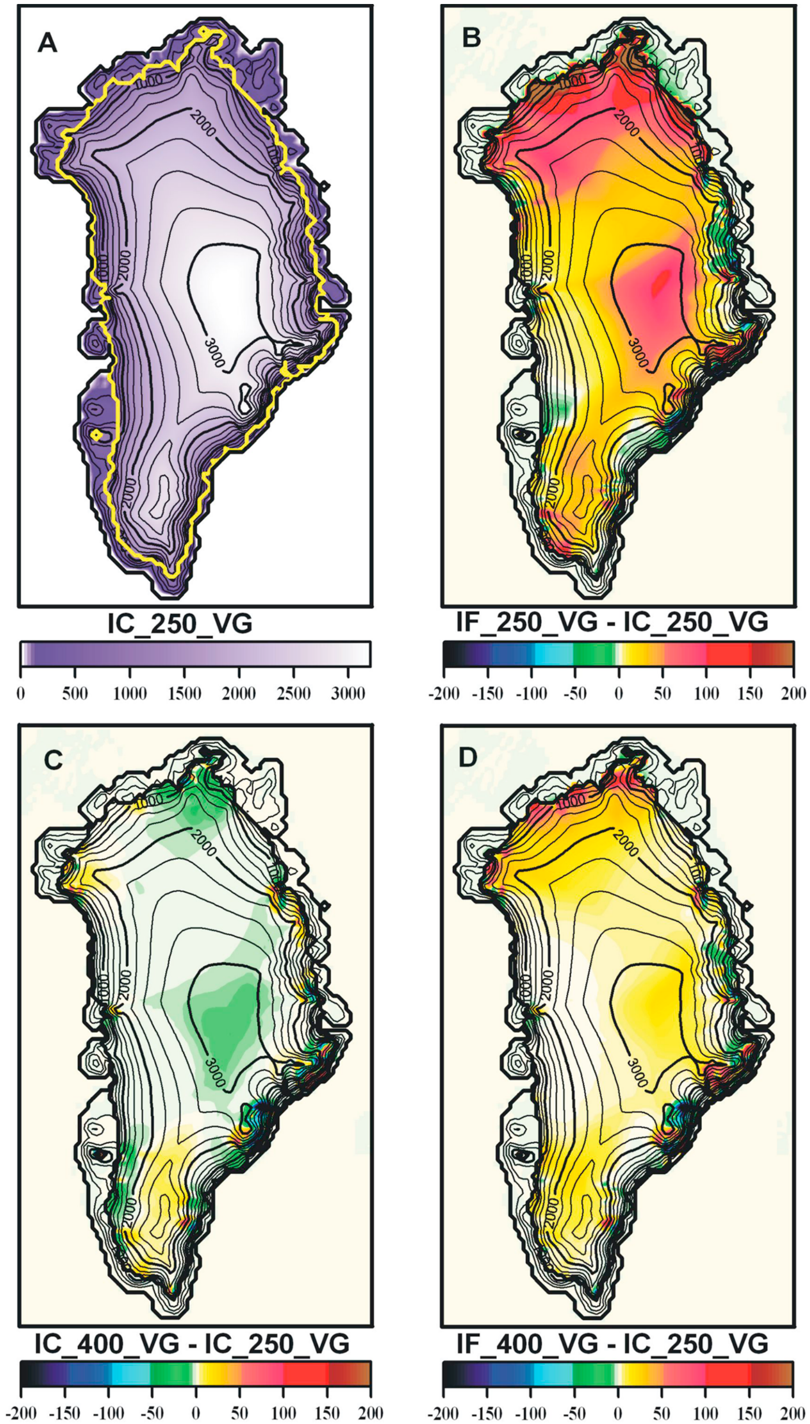

Figure 2. (a) Present-day surface elevation simulated by run IC_250_VG. Yellow contour indicates the ice-land boundary. Departures of the surface elevation computed by runs (b) IF_250_VG, (c) IC_400_VG, and (d) IF_400_VG from that calculated by run IC_250_VG. The superimposed contours are the results from run IC_250_VG.

peratures in the vicinity of the GRIP station are approximately 17.2°C and 5.3°C lower than the present-day temperature. In Figure 3, time series of ice volume and basal temperatures simulated by the transient runs IF_250_VG, IF_240_VG and IF_238_VG are compared with the corresponding time series resulting from the initially ice-covered run IC_400_VG (section 3.1). Figures 3c and 3d show that both the MB temperatures and SMB temperatures simulated by runs IF_240_VG and IF_238_VG are significantly higher than those resulting from run IF_250_VG and closer to the temperatures simulated by the longer simulation (run IC_400_VG). As mentioned previously, the basal temperatures of an ice sheet would be higher than those at its surface, hence the use of initial temperatures that are warmer

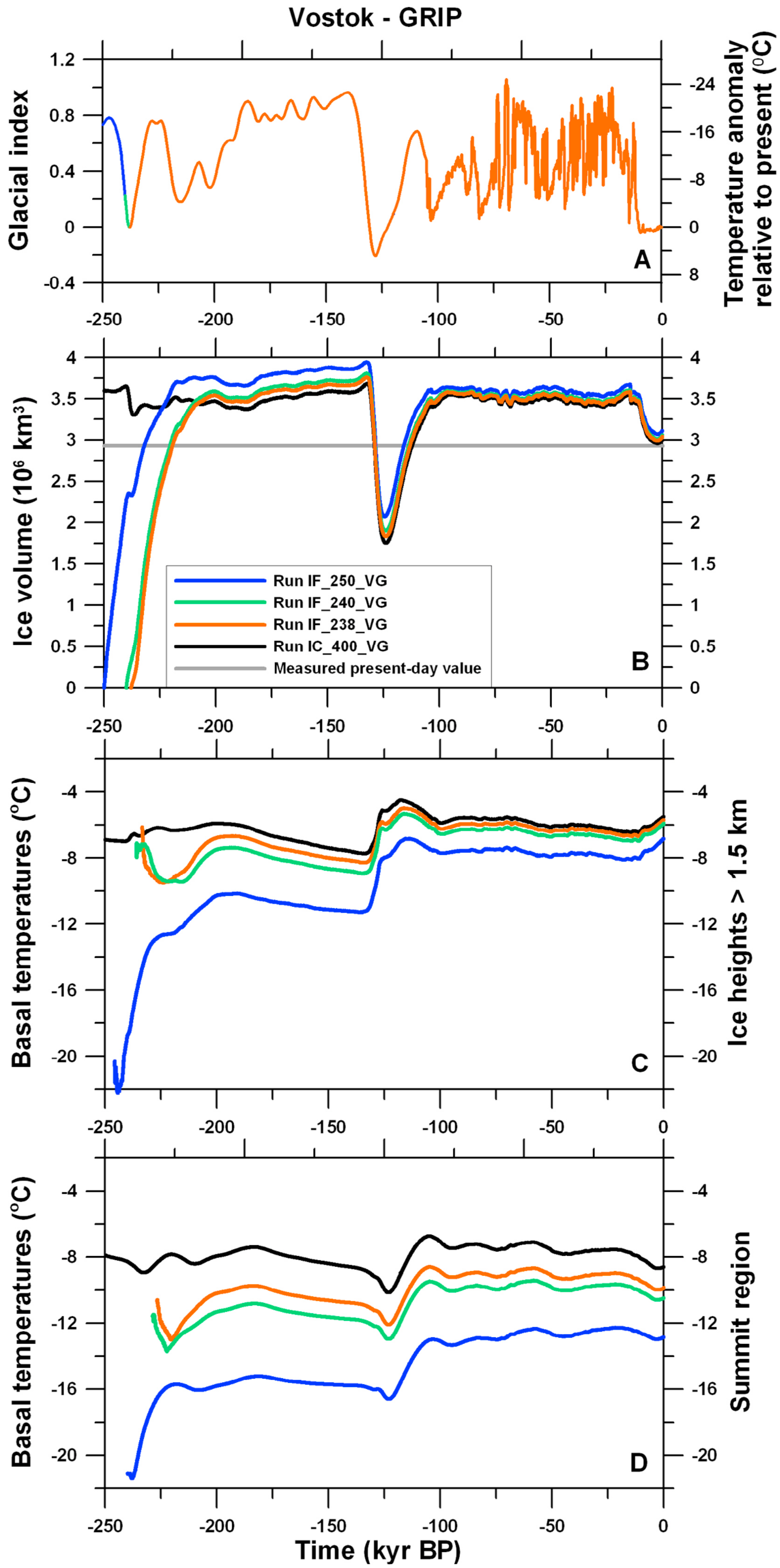

Figure 3. (a) Time-dependent component of atmospheric forcing: glacial index based on a combination of the GRIP and Vostok records [*Greve*, 2005]. (b) Volume changes in the modeled GIS in response to climate variations (transient runs IF_250_VG, IC_400_VG, IF_240_VG, and IF_238_VG; see Table 1). (c) MB temperatures. (d) SMB temperatures.

than those used in run IF_250_VG would be expected to give results closer to those of IC_400_VG.

[24] We thus can see that the choice of the initial climatic conditions in the initially ice-free transient runs may have the same importance on the modeling results as the choice of simulation time. According to Figure 3b, the present-day ice volume computed by the longer simulation IF_250_VG (3.113×10^6 km^3) differs from the observed present-day ice volume (2.93×10^6 km^3) by much more than the corresponding volumes resulting from the shorter simulations IF_240_VG and IF_238_VG (3.053×10^6 km^3 and 3.036×10^6 km^3, respectively). A better agreement can still be obtained by changing the initial state, for instance, by prescribing higher bedrock temperatures, or by letting the initially ice-free simulation proceed for a longer time, as documented by run IF_400_VG in section 3.1.

3.3. Paleoclimatic Versus Steady State Simulations

[25] The aim of this section is to assess the influence of the uncertainties contained in the GRIP ice core record prior to 100 kyr BP on transient simulations of the GIS evolution. For this purpose, we carry out run IC_250_G, which is forced by a glacial index based on only the GRIP ice core record over the entire simulation time from 250 kyr BP to the present (Figure 4, green curves), and compare it to the results from run IC_250_VG (see section 3.1), which is driven by the forcing based on the Vostok and GRIP ice core records (Figure 4, black curves). All runs discussed in this section have as initial conditions the present-day ice-surface and bedrock topographies as described in section 3.1. In many glaciological studies, the initial states for the transient simulations are preinitialized by steady state simulations under past climatic conditions. Therefore, here we also consider such a case, by performing the simulation IC_150_SS_100_G, which is preinitialized by a steady state simulation under conditions as at 100 kyr BP. The steady state simulation is run for 150 kyr (i.e., from 250 to 100 kyr BP). After that, the simulation is driven by the GRIP-based glacial index from 100 kyr BP until today (Figure 4, red curves). Finally, the shortest run, IC_100_G, is conducted to verify our conclusions made in section 3.1 that a simulation time of 100 kyr is sufficiently long for a transient run to mostly forget an unrealistic initial state. Run IC_100_G is driven by the GRIP-based glacial index from 100 kyr BP until the present-day without a preinitialization step (Figure 4, blue curves). Apart from the different states of the GIS at 100 kyr BP, all four runs (IC_250_VG, IC_250_G, IC_150_SS_100_G and IC_100_G) are identical with respect to external forcing and parameters between 100 kyr BP and the present day. The resulting present-day topographies and temperatures of the four transient runs are compared with those obtained by the steady state simulation IC_250_SS under present-day conditions, for which the glacial index is kept constant and equal to 0 until the steady state is reached (Figure 4, orange curves).

[26] Figure 4 shows that, even after 100 kyr of simulations driven by the same external forcing, the present-day volumes (3.002×10^6 km^3, 2.989×10^6 km^3, 2.972×10^6 km^3 and 3.005×10^6 km^3) and the present-day MB and SMB temperatures computed by the transient runs IC_250_VG, IC_250_G, IC_150_SS_100_G and IC_100_G, respectively, still differ from each other. To estimate the range of misfit between each couple of evolving ice sheets, we perform a run-similarity analysis between runs i and j using a misfit function Ψ_{ij} which is defined as

$$\Psi_{ij} = \frac{1}{7}\left[\left|1-\frac{V_i}{V_j}\right| + \left|1-\frac{A_i}{A_j}\right| + \left|1-\frac{T_i^m}{T_j^m}\right| + \left|1-\frac{T_i^b}{T_j^b}\right| + \left|1-\frac{v_i^m}{v_j^m}\right| + \left|1-\frac{v_i^b}{v_j^b}\right| + \left|1-\frac{v_i^z}{v_j^z}\right|\right] \times 100\%, \quad (1)$$

where V_i, A_i, T_i^m, T_i^b, v_i^m, v_i^b, and v_i^z are the ice volume, ice-covered area, mean temperature averaged over the whole ice sheet, MB temperature, mean velocity, mean basal velocity and mean vertical velocity, respectively, computed by run i. Mean velocities are calculated from the horizontal and vertical velocities as

$$v_i^m = \frac{1}{|\{x\}|} \times \frac{1}{|\{y\}|} \times \frac{1}{|\{z\}|} \times \sum_{\{x\}}\sum_{\{y\}}\sum_{\{z\}} \sqrt{v_x^2(x,y,z) + v_y^2(x,y,z) + v_z^2(x,y,z)}, \quad (2)$$

where $\{x\}$,{y} and {z} are the sets of all grid points in the x, y and z directions, respectively, over which the mean value is calculated; $|\{x\}|$, |{y}| and |{z}| are the total numbers of grid points in the sets $\{x\}$, {y} and {z}, respectively; and $v_x(x,y,z)$ and $v_y(x,y,z)$ are the horizontal velocities and $v_z(x,y,z)$ is the vertical velocity.

[27] The misfit function Ψ_{ij} estimates the differences between both the geometrical quantities such as ice volume and ice-covered area and the field quantities such as temperature and velocity. We postulate that two runs perform similarly if Ψ_{ij} does not exceed 1%. Although the choice of a 1% limit (Figure 5) is somewhat arbitrary, it nonetheless indicates that a very good fit between two runs is achieved, while from experience a better agreement between runs is rarely reached.

[28] The misfit between runs IC_250_VG and IC_250_G (Figure 5, black curve) is about 6% at 100 kyr BP, improving to less than 1% after only 30 kyr (i.e., at 70 kyr BP). A misfit of 1% between runs IC_250_G and IC_150_SS_100_G (Figure 5, violet curve) is accomplished even faster, by 80 kyr BP. On the other hand, a 1% misfit is not reached by runs IC_250_VG and IC_150_SS_100_G (Figure 5, light blue curve) within the entire 100 kyr simulation. The two types of climatic forcing used to preinitialize the GIS states at 100 kyr BP in runs IC_250_VG (Vostok and GRIP) and IC_250_G (GRIP only) have quite different amplitudes describing climate variability over the Summit region (Figure 4a). For example, the glacial index used as a forcing in run IC_250_G prior to 100 kyr BP does not contain the rapid and steep variations that are present in the glacial index based on the Vostok ice core record. The forcing of run IC_250_G is therefore much closer to the constant forcing employed in run IC_150_SS_100_G between 250 and 100 kyr BP. The shortest run, IC_100_G, reaches 1% misfit with run IC_250_VG (Figure 5, green curve) shortly before the Holocene (13 kyr BP or after 87 kyr of simulation), attaining this with runs IC_250_G (Figure 5, red curve) and SS_100_G (Figure 5, dark blue curve) even later, during the Holocene (8 kyr BP or after 92 kyr of simulation).

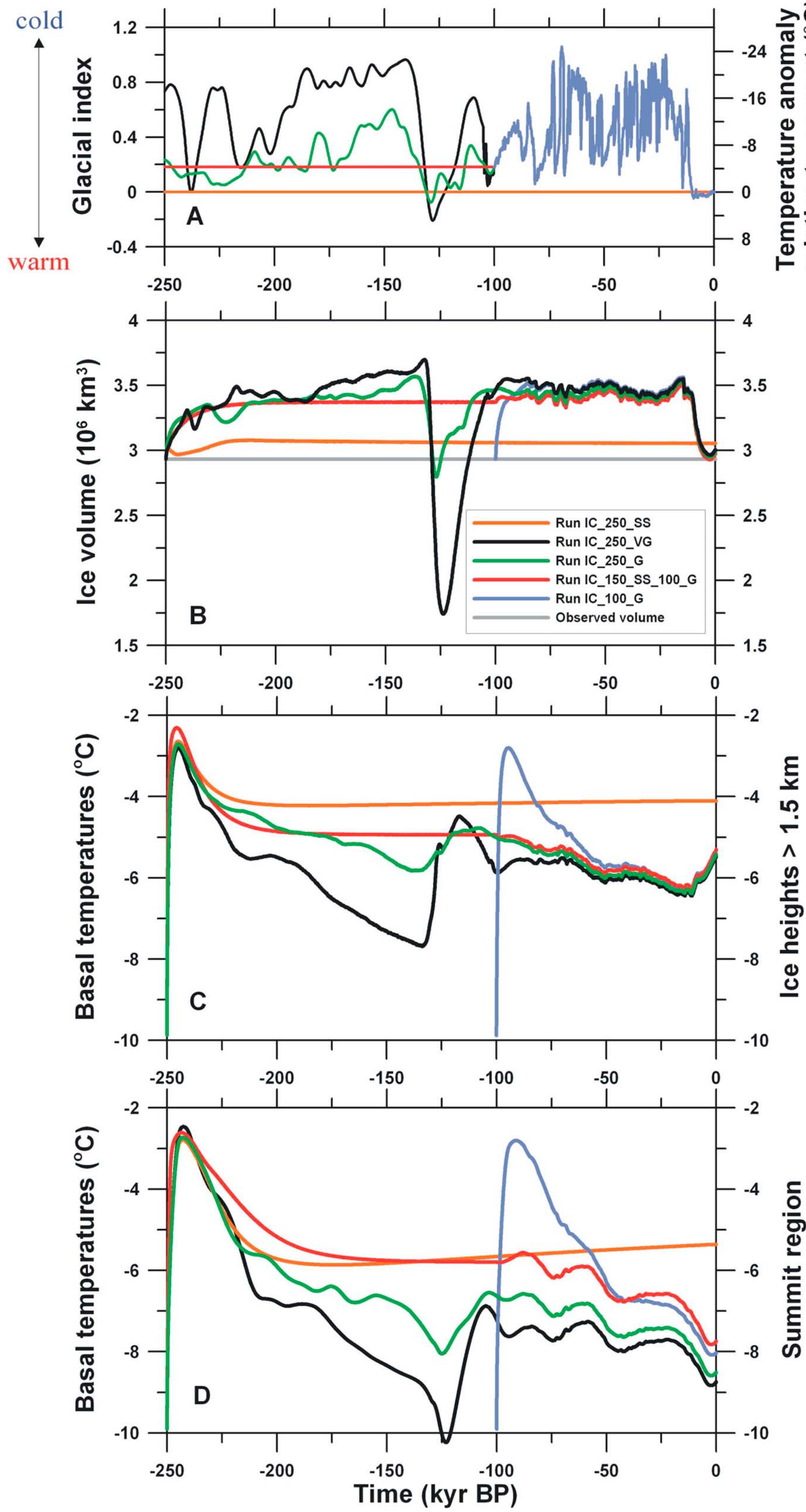

Figure 4. (a) Time-dependent component of atmospheric forcing (glacial index) for runs IC_250_SS, IC_250_VG, IC_250_G, IC_150_SS_100_G, and IC_100_G (see Table 1). (b) Volume changes of the modeled GIS in response to climate change. (c) MB temperatures. (d) SMB temperatures.

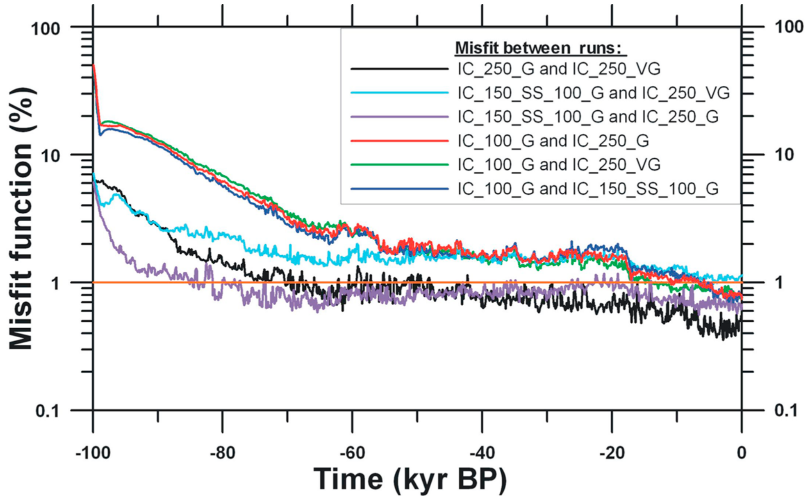

Figure 5. Misfit between each couple of paleoclimatic runs (percent): equation (1) as applied to the general quantities of the ice sheets computed by each pair of transient runs in order to estimate the range of differences in ice volumes, areas covered by the modeled ice sheet, mean temperatures, mean velocities, MB temperatures, and MB velocities, simultaneously.

[29] Inspecting the SMB temperatures in Figure 4d, we can observe that, while runs IC_250_VG and IC_250_G arrive at nearly the same temperatures, with a difference of only 0.2°C, the temperatures resulting from the other two transient runs are approximately 1°C higher. However, the MB and SMB temperatures computed by the steady state run IC_250_SS are 1.3°C and 2.4°–3.4°C higher, respectively, than those resulting from the four transient runs. Moreover, the SMB temperature continues to increase even after 250 kyr of steady state simulation, which does not conform to the common assumption that a 100 kyr (or even 50 kyr) period of initialization is sufficient to reach a steady state [*Calov and Hutter*, 1996; *Charbit et al.*, 2007; *Greve*, 1997b;

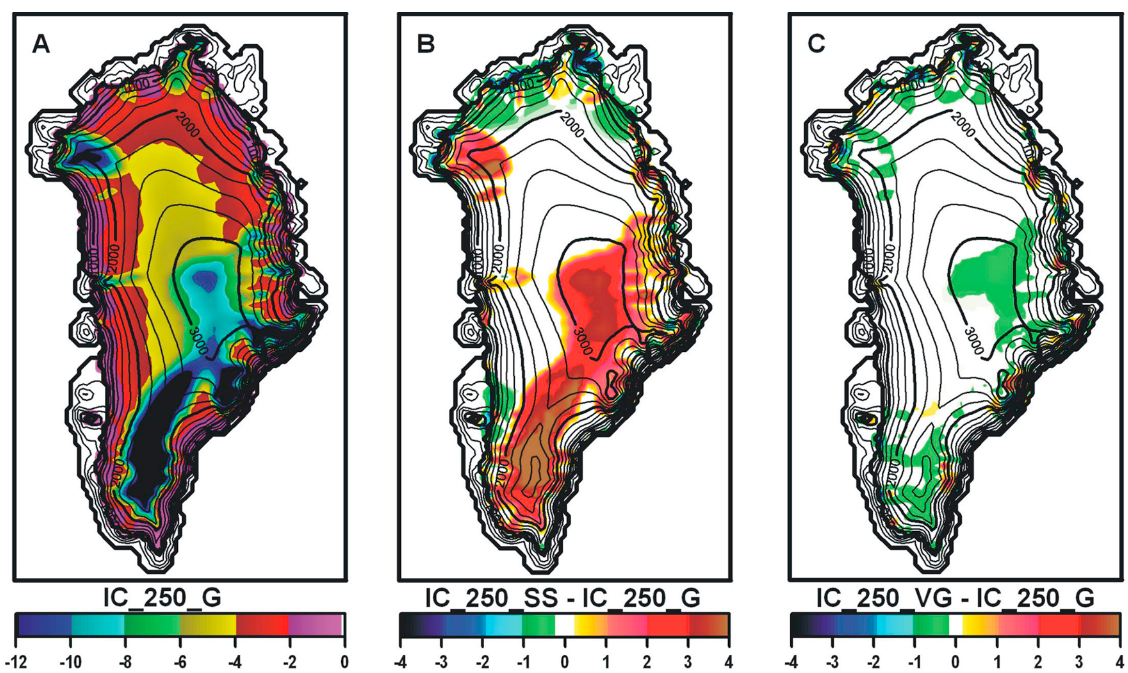

Figure 6. (a) Present-day basal temperatures (degrees Celsius) of the ice sheet as computed by run IC_250_G (transient simulation driven by only the GRIP record). (b) Differences between the present-day basal temperatures computed by run IC_250_SS (steady state simulation) and run IC_250_G. Black borders denote the edges of the ice-covered area (dashed correspond to run IC_250_SS and solid correspond to run IC_250_G) and the costal line. (c) Differences between simulated present-day basal temperatures computed by run IC_250_VG (prior to 100 kyr BP preinitialized using atmospheric forcing based on the Vostok record, then forced by the GRIP record) and run IC_250_G.

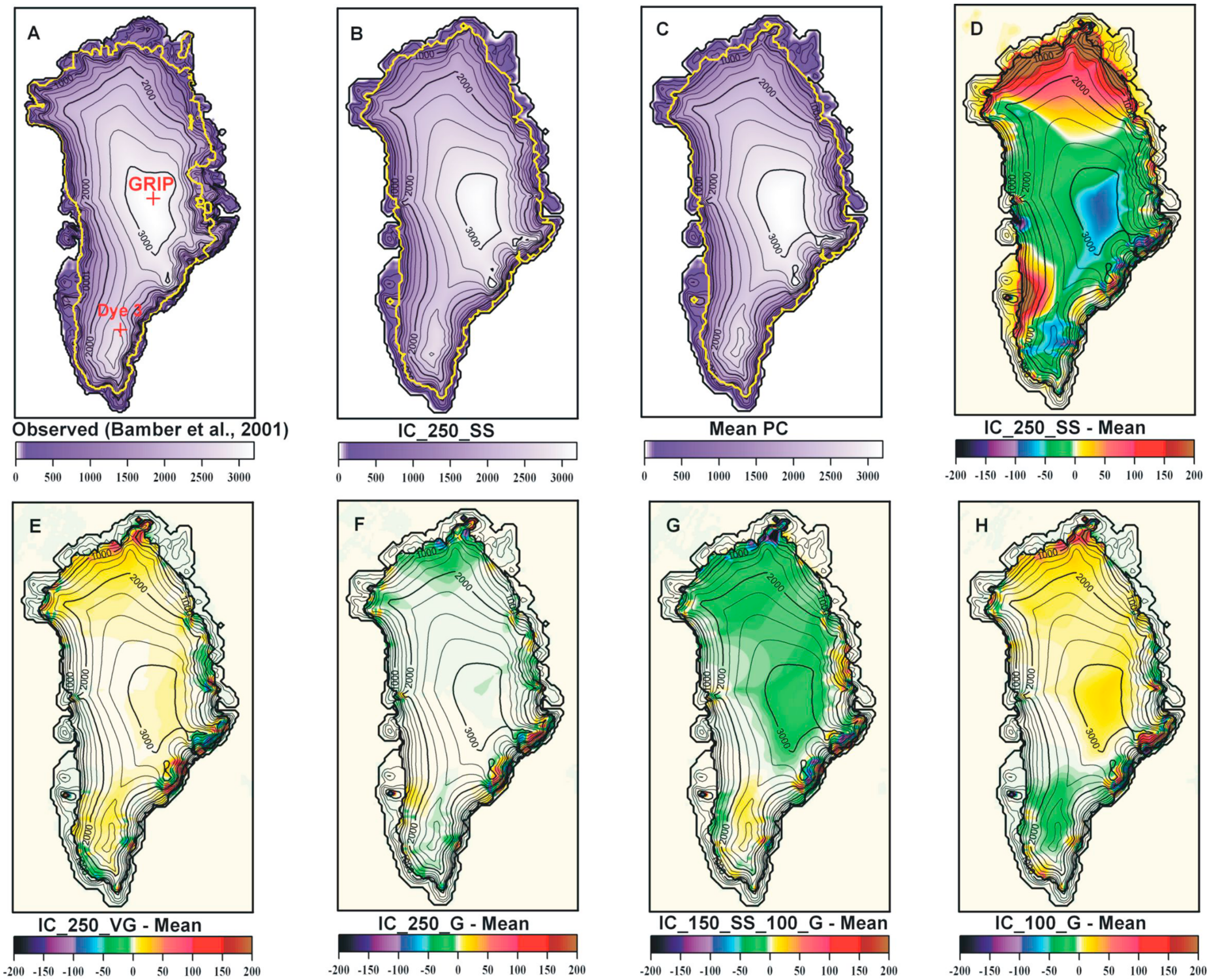

Figure 7. (a) Observed present-day surface elevation [*Bamber et al.*, 2001; *Layberry and Bamber*, 2001]. (b) Present-day surface elevation computed by the steady state simulation (run IC_250_SS). (c) Mean values calculated based on the present-day surface elevation fields computed by transient simulations (runs IC_250_VG, IC_250_G, IC_150_SS_100_G, and IC_100_G). (d) Differences between the present-day surface elevations computed by the steady state run IC_250_SS and the mean values shown in Figure 7c. Departures of the present-day surface elevation computed by runs (e) IC_250_VG, (f) IC_250_G, (g) IC_150_SS_100_G, and (h) IC_100_G from the mean topography shown in Figure 7c. Yellow contours indicate the observed and modeled ice-land boundaries.

Greve et al., 1999a; *Huybrechts and T'siobbel*, 1995; *Letreguilly et al.*, 1991; *Ritz et al.*, 1997, 2001; *Takeda et al.*, 2002].

[30] Figure 6 presents the differences in the modeled present-day basal temperatures computed by the steady state run IC_250_SS (Figure 6b) and the transient run IC_250_VG (Figure 6c) with respect to the results of run IC_250_G (Figure 6a). We now have evidence that the temperature of basal ice layers as determined by the steady state simulation IC_250_SS are significantly warmer (by up to 4.5°C) over the area between the GRIP Summit site and the southern summit at the Dye-3 station (the locations of these stations are indicated in Figure 7a). The steady state simulation results in a more uniform distribution of basal temperatures than the transient runs, evident by the steady state basal temperatures being significantly higher than those from the transient run for all areas with the lower ice temperatures. At the same time, the differences in basal temperatures computed by runs IC_250_VG and IC_250_G do not exceed 0.3°C except for the local areas at the margins of the ice sheets (Figure 6c).

[31] Figure 7 compares the modeled present-day topographies with the observed topography (Figure 7a), where Figure 7b is the topography from the steady state run IC_250_SS and Figure 7c is the mean topography from the results of the four transient simulations considered in this section (IC_250_VG, IC_250_G, IC_150_SS_100 and IC_100_G). Figure 7d shows the difference between the ice-surface topography resulting from the steady state simulation IC_250_SS and the mean topography. Comparing Figures 7d and 6b (the difference in basal temperatures between the steady state IC_250_SS and transient IC_250_G runs), we observe that the differences in the basal temperatures are strongly correlated with the differences in the ice-

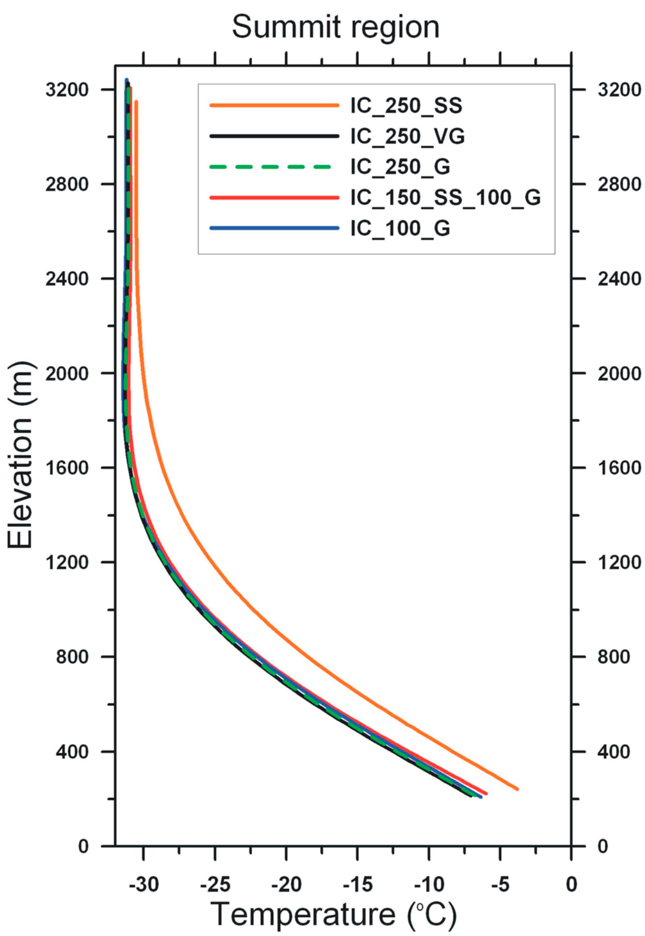

Figure 8. Temperature profiles averaged over the Summit region. Simulated present-day temperatures resulting from run IC_250_SS (steady state simulation) are compared with the temperatures obtained from the transient simulations (runs IC_250_VG, IC_250_G, IC_150_SS_100_G, and IC_100_G).

surface topographies. Hence, the precise modeling of the basal temperatures is closely related to the modeling of the present-day ice-surface topography, as documented by *Greve* [2005] and *Tarasov and Peltier* [2003].

[32] Figures 7e–7h show the departures of the ice-surface topographies computed by each of the four transient runs from the mean topography. The differences between the topography computed by run IC_250_VG and the mean topography (Figure 7e) are quite small, exceeding 20 m only at the edges of the ice sheet. Topography resulting from run IC_250_G (Figure 7f) almost coincides with the mean topography, again except for the margins and the most northern part of the GIS. As for the topographies resulting from runs IC_150_SS_100_G and IC_100_G, their departures from the mean values (Figures 7g and 7h, respectively) cover much larger areas and reach about 30–40 m, but in the opposite directions with the IC_150_SS_100_G topography being lower than the mean, and the IC_100_G topography being greater. This means the differences between the final results of these two runs are twice as large as their departures from the mean topography. We therefore conclude that the uncertainties in the GIS state at 100 kyr BP exert the largest influence on the modeled present-day ice-surface topographies in the northern and central areas of the modeled GIS, reaching a maximum of 80 m, corresponding to a difference of about 5.5–10% and 2.5–3% in the ice heights of these regions, respectively.

[33] *Greve* [1997c] and *Greve et al.* [1999a] compared depth profiles of measured and simulated temperatures from the GRIP and GISP2 ice cores (both located in the Summit region, separated by a distance of 28 km) and found that their simulated values conformed to the measured ones at both locations. In the work by *Greve* [1997c], the present-day GIS was initialized by paleoclimatic simulations similar to IC_250_G, while in the work by *Greve et al.* [1999a], the initial state at 250 kyr BP was additionally preinitialized by a steady state run under the same climatic conditions as at 250 kyr BP. They then compared the vertical profiles of measured temperatures from the GRIP and GISP-2 ice core locations [*Cuffey et al.*, 1995; *Johnsen et al.*, 1995] with the results of a paleoclimatic simulation. We now analyze similar temperature profiles from the present-day results of the transient runs IC_250_VG, IC_250_G, IC_150_SS_100_G and IC_100_G and the steady state run IC_250_SS (Figure 8). The temperatures are found by averaging over the Summit region at each depth. We note that the resulting temperature profiles are similar for all four transient runs, although the temperatures resulting from run IC_100_G are slightly higher. On the other hand, the temperatures computed by the steady state run IC_250_SS are 3–4°C higher than those from the transient runs, which is in agreement with the conclusion of *Dahl-Jensen and Johnsen* [1986] concerning the difference between the temperatures computed by the 2-D steady state and transient simulations in the area of the Dye-3 ice core (see Figure 7a for the location of the Dye-3 ice core). In Figure 8, a relatively good agreement between the profiles from the steady state and transient runs can only be seen for the ice layers at elevations above 2400 m.

[34] Figure 9 presents an east-west cross section of temperatures $T' = T - T_{melt}$ through the ice sheet (taking in the location of the GRIP ice core) where T is the temperature of the ice and T_{melt} is the temperature at the pressure melting point. We note that even the uppermost ice layers computed by run IC_250_SS (Figure 9, bottom) are warmer than those resulting from the transient runs (Figure 9, top). This can be explained by the fact that the temperature profiles computed by paleoclimatic runs reflect the climate history, whereas the climatic conditions in the steady state simulation are kept constant and are significantly warmer than those during glacial periods. Such differences in the thermodynamic states of the modeled GIS may affect the dynamics of the entire ice sheet over intermediate and long time scales (thousands of years). Since it has been shown that transient runs provide results that fit measured temperatures well [*Greve*, 1997c, *Greve et al.*, 1999a], it is likely that transient runs driven by surface-temperature histories inferred from ice core records would reconstruct the present-day state of the GIS in a more realistic fashion.

4. Conclusions

[35] In this paper, we study the problem of initialization in the modeling of the present-day and past states of the GIS. A series of paleoclimatic simulations with different initial

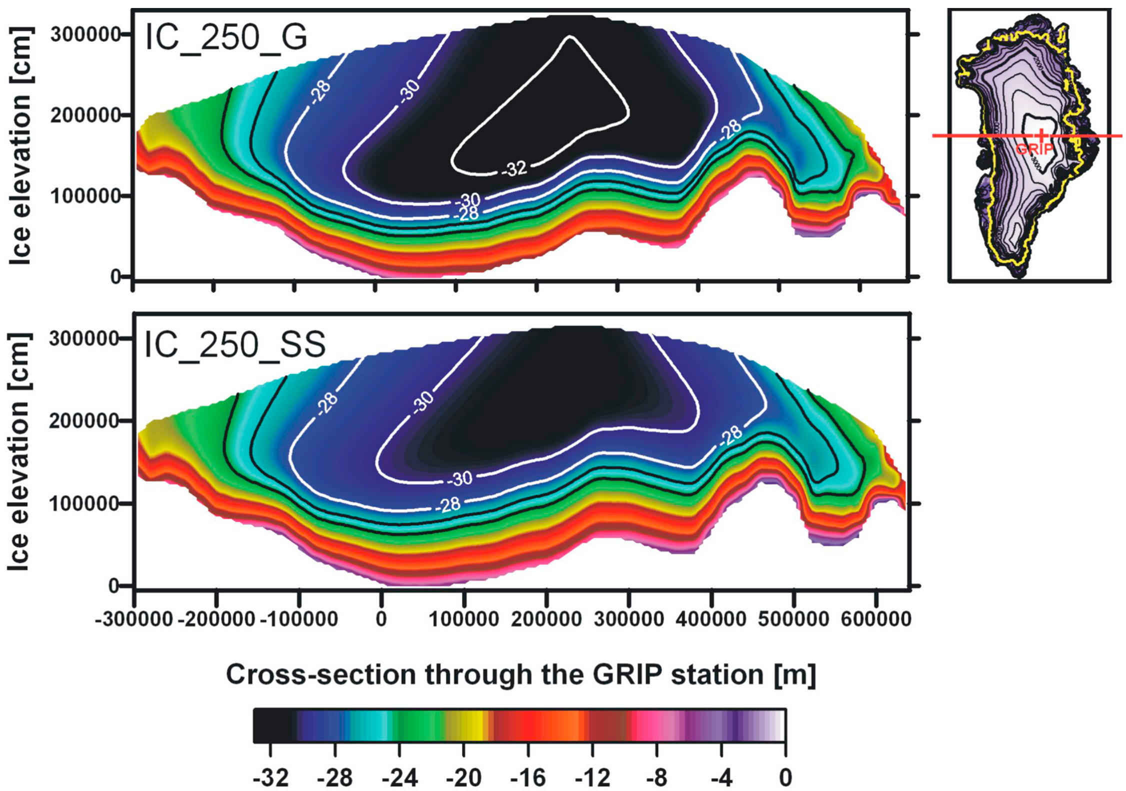

Figure 9. Cross-sectional distribution of temperatures $T' = T - T_{melt}$ obtained from (top) run IC_250_G (transient run driven by the glacial index based on the GRIP ice core record) and (bottom) run SS_250_SS (steady state simulation under the present-day climatic conditions).

conditions, integration lengths and types of climatic forcing is performed in order to obtain some measure of the differences between the ice sheet topographies and temperatures computed by various transient runs. We particularly focus on the evolution of the basal ice temperatures, since this quantity represents the ice sheet's longest memory.

[36] We find that the choice of ice-covered initial conditions potentially significantly shortens the required initialization time. In particular, 100 kyr of simulation, starting from the present-day ice-surface and bedrock topographies without an additional spin-up, is sufficient to fit very well the results of paleoclimatic runs with longer simulation times. A slight improvement in the agreement between the simulated and observed ice volumes can be further achieved by prolonging the simulation time.

[37] On the other hand, transient simulations with ice-free initial conditions arrive at a 1–5% worse fit between the modeled and observed ice volumes. Moreover, the thermodynamic states of the GIS modeled by ice-free runs are strongly dependent on the choice of initial air temperatures. We demonstrate that a glacial climate is an unfavorable choice of start-up condition for initially ice-free simulations because the thermodynamic state of the resulting ice sheet is significantly affected by the extremely low temperatures of the modeled bedrock and the newly accumulated snow (i.e., much colder than for an existing ice sheet). As a result, such simulations give larger errors in the ice sheet's thermodynamic state and ice-surface topography compared with observations.

[38] We also study the influence of the uncertainties affecting the GRIP ice core record prior to 100 kyr BP. For this purpose, we perform a series of runs driven by atmospheric forcing based on a 100 kyr reconstruction of temperature history obtained from the GRIP ice core record and various types of forcing prior to 100 kyr BP. We find substantial differences in the dynamic and thermodynamic states of the ice sheets generated by the spin-up simulations when driven by Vostok- or GRIP-based forcing prior to 100 kyr BP. However, the two preinitialized ice sheets reach similar states after 30–40 kyr of further simulations driven by GRIP-based forcing. The differences in the resulting present-day topographies of 10–30 m and temperature differences of a maximum of 0.3°C could be considered as being negligible, although the basal layers still partly remember different initial states.

[39] Finally, the present-day thermodynamic states and topographies of the ice sheets obtained from the transient runs are compared with those resulting from the steady state simulation. The comparison of ice temperatures shows large differences of up to 4.5°C, such that the ice sheet initialized by the steady state simulation is overall warmer than those generated by paleoclimatic simulations (see Figures 8 and 9). These significant differences in ice temperatures caution against the use of steady state simulations as the initialization technique for modeling the present-day GIS.

Appendix A: Model Equations for the Cold-Ice Method

[40] The complete set of field equations and boundary conditions can be found in the work by *Greve* [1995,

1997a]. Here, we only present the main prognostic equations for the case of the cold-ice method.

[41] The equation for ice thickness is given by

$$\frac{\partial H}{\partial t} = \frac{\partial (h-b)}{\partial t} = -\frac{\partial q_x}{\partial x} - \frac{\partial q_y}{\partial y} + a_s - \frac{P_b}{\rho}, \qquad \text{(A1)}$$

where x and y are the horizontal Cartesian coordinates, z is the vertical Cartesian coordinate defined as elevation above sea level, t is the time, h is the z coordinate of the ice surface, b is the z coordinate of the ice base (lithosphere surface), H is the ice thickness, q_x and q_y are the components of the horizontal mass flux, a_s is the accumulation-ablation function at the ice surface, P_b is the basal melting rate, and ρ is the density of ice. The equation for the bedrock response to changing ice loads is expressed as

$$\frac{\partial b}{\partial t} = -\frac{1}{\tau_\nu}\left[b - \left(b_0 - \frac{\rho}{\rho_a}H\right)\right], \qquad \text{(A2)}$$

where τ_ν is the time lag for the lithosphere response, b_0 is the position of b for the relaxed lithosphere surface without ice load, and ρ_a is the density of the asthenosphere.

[42] The temperature equation for cold ice regions is

$$\frac{\partial T}{\partial t} + v_x\frac{\partial T}{\partial x} + v_y\frac{\partial T}{\partial y} + v_z\frac{\partial T}{\partial z} = \frac{1}{\rho c}\left[\frac{\partial}{\partial z}\left(\kappa\frac{\partial T}{\partial z}\right) + 2EA(T')f(\sigma)\sigma^2\right], \qquad \text{(A3)}$$

where T is the temperature; v_x, v_y, and v_z are the components of ice velocity; c is the specific heat of ice; κ is the heat conductivity of ice; E is the creep enhancement factor; $A(T')$ is the rate factor for cold ice, dependent upon temperature $T' = T - T_{melt}$, where T is the temperature of the ice and T_{melt} is the temperature at the pressure melting point; and $f(\sigma)$ is the creep function for cold ice, dependent upon the effective shear stress σ. The age of the ice is expressed as

$$\frac{\partial A}{\partial t} + v_x\frac{\partial A}{\partial x} + v_y\frac{\partial A}{\partial y} + v_z\frac{\partial A}{\partial z} = 1\ \left[+D_A\frac{\partial^2 A}{\partial z^2}\right], \qquad \text{(A4)}$$

where A is the age of the ice and D_A is the numerical diffusivity, which is needed for reasons of numerical stability. The temperature equation for the lithosphere is given by

$$\frac{\partial T}{\partial t} + \frac{\partial b}{\partial t}\frac{\partial T}{\partial z} = \frac{\kappa_r}{\rho_r c_r}\frac{\partial^2 T}{\partial z^2}, \qquad \text{(A5)}$$

where κ_r is the heat conductivity of the lithosphere, ρ_r is the density of the lithosphere, and c_r is the specific heat of the lithosphere.

Appendix B: Climatic Forcing

[43] The mean annual and July surface temperatures are parameterized by

$$T_{ma}(\theta,\varphi,t) = T_{ma\_present}(\theta,\varphi) + g(t)\cdot\Delta T_{ma\_LGM}(\theta,\varphi) \qquad \text{(B1)}$$

$$T_{mj}(\theta,\varphi,t) = T_{mj\_present}(\theta,\varphi) + g(t)\cdot\Delta T_{mj\_LGM}(\theta,\varphi), \qquad \text{(B2)}$$

where ΔT_{ma_LGM} and ΔT_{mj_LGM} are the mean annual and mean July LGM temperature anomalies, respectively; θ and φ are latitude and longitude, respectively; and $g(t)$ is the glacial index (see section 2.2). The present-day surface temperatures $T_{ma\_present}$ and $T_{mj\_present}$ are based on the parameterization by *Ritz et al.* [1997] fitting the observed present-day temperature fields. Monthly temperatures are calculated assuming a sinusoidal annual cycle, given by

$$T_{mm}(\theta,\phi,t,n) = T_{ma}(\theta,\phi,t) + \sin\left(\frac{(n-4)}{6}\pi\right) \times \left(T_{mj}(\theta,\phi,t) - T_{ma}(\theta,\phi,t)\right), \qquad \text{(B3)}$$

where n = [1,…,12] is the number of the month.

[44] Mean annual precipitation rates are computed as

$$P_{ma}(\theta,\phi,t) = P_{ma\_present}(\theta,\phi) \times (\Delta P_{ma\_LGM}(\theta,\phi))^{g(t)}, \qquad \text{(B4)}$$

where $\Delta P_{ma\_LGM}(\theta, \varphi)$ is the LGM anomaly of the rate of precipitation. The present-day mean annual precipitation rates $P_{ma\_present}$ are based on the digitized accumulation map of *Calanca et al.* [2000]. Mean monthly precipitation rates are assumed to be equal to the mean annual rates and are converted into snowfall based on the relation by *Marsiat* [1994]:

$$S_{mm}(\theta,\phi,t,n) = P_{ma}(\theta,\phi,t) \times \begin{cases} 0, & T_{mm}(\theta,\varphi,t,n) \geq T_{rain} \\ \dfrac{T_{rain} - T_{mm}(\theta,\phi,t,n)}{T_{rain} - T_{snow}}, & T_{snow} \leq T_{mm}(\theta,\varphi,t,n) \leq T_{rain} \\ 1, & T_{mm}(\theta,\varphi,t,n) \leq T_{snow} \end{cases}, \qquad \text{(B5)}$$

where T_{snow} = −10°C and T_{rain} = +7°C.

Appendix C: Enhancement Factor

[45] In the present-day steady state simulations, the enhancement factor E is given by

$$E = \begin{cases} 1, & 0 < A < 11 \\ 3, & A \geq 11 \end{cases}, \qquad \text{(C1)}$$

where A is age of the ice in kyr. In the transient simulations, it is given by

$$E = \begin{cases} 3, & t_{acc} < -132 \\ 1, & -132 \leq t_{acc} < -114.5 \\ 3, & -114.5 \leq t_{acc} < -11 \\ 1, & t_{acc} \geq -11 \end{cases}, \qquad \text{(C2)}$$

where the accumulation time $t_{acc} = t - A$ denotes the moment when an ice particle has been deposited on the surface of the ice sheet. The accumulation time $t_{acc} < -132$ kyr means that the ice particle was accumulated during the pre-Eemian time, $-132 \leq t_{acc} < -114.5$ was accumulated during the Eemian period, $-114.5 \leq t_{acc} < -11$ was accumulated during the Wisconsin period, and $t_{acc} \geq -11$ was accumulated during the Holocene period.

[46] **Acknowledgments.** Irina Rogozhina is grateful to Ralf Greve for providing access to his numerical code SICOPOLIS: without his ice sheet model, this research would not have been possible. All authors of this paper are especially grateful to Reinhard Calov for his readiness to explain how SICOPOLIS is made up and how to tame it and, moreover, for his invaluable recommendations on how to improve this paper. We are thankful to James Fastook and an anonymous reviewer for their incredibly positive reviews and to the Associate Editor and another anonymous reviewer for their helpful remarks. Zdenek Martinec acknowledges the support from the Grant Agency of the Czech Republic through grant 205/09/0546. Kevin Fleming acknowledges the support of the Australian Research Council's *Discovery Projects* funding scheme (project DP087738).

References

Abe-Ouchi, A., S. Segawa, and F. Saito (2007), Climatic conditions for modelling the Northern Hemisphere ice sheets throughout the ice age cycle, *Clim. Past*, *3*, 423–438, doi:10.5194/cp-3-423-2007.

Alley, R. B., et al. (1993), Abrupt increase in Greenland snow accumulation at the end of the Younger Dryas event, *Nature*, *362*, 527–529, doi:10.1038/362527a0.

Andersen, K. K., et al. (2004), High-resolution record of Northern Hemisphere climate extending into the last interglacial period, *Nature*, *431*(7005), 147–151, doi:10.1038/nature02805.

Arthern, R. J., and G. H. Gudmundsson (2010), Initialization of ice-sheet forecasts viewed as an inverse Robin problem, *Ann. Glaciol.*, *56*, 527–533, doi:10.3189/002214310792447699.

Arthern, R. J., and R. C. A. Hindmarsh (2006), Determining the contribution of Antarctica to sea-level rise using data assimilation methods, *Philos. Trans. R. Soc. A*, *364*, 1841–1865, doi:10.1098/rsta.2006.1801.

Baldwin, D. J., J. L. Bamber, A. J. Payne, and R. L. Layberry (2003), Using internal layers from the Greenland Ice Sheet, identified from radio echo sounding data, with numerical models, *Ann. Glaciol.*, *37*, 325–330, doi:10.3189/172756403781815438.

Bamber, J. L., R. L. Layberry, and S. P. Gogineni (2001), A new ice thickness and bed data set for the Greenland ice sheet: 1. Measurement, data reduction, and errors, *J. Geophys. Res.*, *106*, 33,773–33,780, doi:10.1029/2001JD900054.

Budd, W. F., B. Coutts, and R. C. Warner (1998), Modelling the Antarctic and northern-hemisphere ice-sheet changes with global climate through the glacial cycle, *Ann. Glaciol.*, *27*, 153–160.

Bueler, E., C. S. Lingle, J. A. Kallen-Brown, D. N. Covey, and L. N. Bowman (2005), Exact solutions and verification of numerical models for isothermal ice sheets, *J. Glaciol.*, *51*, 291–306, doi:10.3189/172756505781829449.

Calanca, P., H. Gilgen, S. Ekholm, and A. Ohmura (2000), Gridded temperature and accumulation distributions for use in cryospheric models, *Ann. Glaciol.*, *31*, 118–120, doi:10.3189/172756400781820345.

Calov, R. (2006), Modelling of terrestrial ice sheets in palaeo-climate research, *GAMM-Mitt.*, *29*(1), 9–28.

Calov, R., and R. Greve (2005), A semi-analytical solution for the positive degree-day model with stochastic temperature variations, *J. Glaciol.*, *51*, 173–175.

Calov, R., and K. Hutter (1996), The thermomechanical response of the Greenland ice sheet to various climate scenarios, *Clim. Dyn.*, *12*, 243–260, doi:10.1007/BF00219499.

Calov, R., A. Ganopolski, M. Claussen, V. Petoukhov, and R. Greve (2005a), Transient simulation of the last glacial inception. Part I: Glacial inception as a bifurcation of the climate system, *Clim. Dyn.*, *24*, 545–561, doi:10.1007/s00382-005-0007-6.

Calov, R., A. Ganopolski, V. Petoukhov, M. Claussen, V. Brovkin, and C. Kubatzki (2005b), Transient simulation of last glacial inception. Part II: Sensitivity and feedback analysis, *Clim. Dyn.*, *24*, 563–576, doi:10.1007/s00382-005-0008-5.

Charbit, S., C. Ritz, and G. Ramstein (2002), Simulations of Northern Hemisphere ice-sheet retreat: Sensitivity to physical mechanisms involved during the Last Deglaciation, *Quat. Sci. Rev.*, *21*(1–3), 243–265, doi:10.1016/S0277-3791(01)00093-2.

Charbit, S., C. Ritz, G. Philippon, V. Peyaud, and M. Kageyama (2007), Numerical reconstructions of the Northern Hemisphere ice sheets through the last glacial-interglacial cycle, *Clim. Past*, *3*, 15–37, doi:10.5194/cp-3-15-2007.

Cuffey, K. M., G. D. Clow, R. B. Alley, M. Stuiver, E. D. Waddington, and R. W. Saltus (1995), Large Arctic temperature change at the Wisconsin-Holocene glacial transition, *Science*, *270*, 455–458, doi:10.1126/science.270.5235.455.

Dahl-Jensen, D., and S. J. Johnsen (1986), Paleotemperatures still exist in the Greenland ice sheet, *Nature*, *320*, 250–252, doi:10.1038/320250a0.

Dansgaard, W., et al. (1993), Evidence for general instability of past climate from a 250-kyr ice-core record, *Nature*, *364*(6434), 218–220, doi:10.1038/364218a0.

Etheridge, D. M., L. P. Steele, R. J. Francey, and R. L. Langenfields (1998), Atmospheric methane between 1000 A.D. and present: Evidence of anthropogenic emissions and climatic variability, *J. Geophys. Res.*, *103*, 15,979–15,993, doi:10.1029/98JD00923.

Forsström, P. L., and R. Greve (2004), Simulation of the Eurasian ice sheet dynamics during the last glaciation, *Global Planet. Change*, *42*(1–4), 59–81, doi:10.1016/j.gloplacha.2003.11.003.

Forsström, P. L., O. Sallasmaa, R. Greve, and T. Zwinger (2003), Simulation of fast-flow features of the Fennoscandian ice sheet during the Last Glacial Maximum, *Ann. Glaciol.*, *37*, 383–389, doi:10.3189/172756403781815500.

Greve, R. (1995), Thermomechanisches Verhalten polythermer Eisschilde-Theorie, Analytik, Numerik, Ph.D. thesis, Dep. of Mech., Darmstadt Univ. of Technol., Darmstadt, Germany.

Greve, R. (1997a), A continuum-mechanical formulation for shallow polythermal ice sheets, *Philos. Trans. R. Soc. London, Ser. A*, *355*, 921–974, doi:10.1098/rsta.1997.0050.

Greve, R. (1997b), Application of a polythermal three-dimensional ice sheet model to the Greenland ice sheet: Response to steady-state and transient climate scenarios, *J. Clim.*, *10*(5), 901–918, doi:10.1175/1520-0442(1997)010<0901:AOAPTD>2.0.CO;2.

Greve, R. (1997c), Large-scale ice-sheet modelling as a means of dating deep ice cores in Greenland, *J. Glaciol.*, *43*(144), 307–310.

Greve, R. (2000), On the response of the Greenland ice sheet to greenhouse climate change, *Clim. Change*, *46*(3), 289–303, doi:10.1023/A:1005647226590.

Greve, R. (2001), Glacial isostasy: Models for the response of the Earth to varying ice loads, in *Continuum Mechanics and Applications in Geophysics and the Environment*, edited by B. Straughan et al., pp. 307–325, Springer, Berlin.

Greve, R. (2005), Relation of measured basal temperatures and the spatial distribution of the geothermal heat flux for the Greenland ice sheet, *Ann. Glaciol.*, *42*, 424–432, doi:10.3189/172756405781812510.

Greve, R., M. Weis, and K. Hutter (1998), Palaeoclimatic evolution and present conditions of the Greenland ice sheet in the vicinity of Summit: An approach by large-scale modeling, *Paleoclimates*, *2*(2–3), 133–161.

Greve, R., B. Mügge, D. R. Baral, O. Albrecht, and A. A. Savvin (1999a), Nested high-resolution modelling of the Greenland Summit region, in *Advances in Cold-Region Thermal Engineering and Sciences*, edited by K. Hutter, Y. Wang, and H. Beer, pp. 285–306, Springer, Berlin, doi:10.1007/BFb0104190.

Greve, R., K.-H. Wyrwoll, and A. Eisenhauer (1999b), Deglaciation of the Northern Hemisphere at the onset of the Eemian and Holocene, *Ann. Glaciol.*, *28*, 1–8, doi:10.3189/172756499781821643.

Hammer, C. U., H. B. Clausen, W. Dansgaard, S. J. Johnsen, and N. Reeh (1978), Dating of Greenland ice cores by flow models, isotopes, volcanic debris, and continental dust, *J. Glaciol.*, *20*, 3–26.

Hammer, C. U., H. B. Clausen, W. Dansgaard, A. Neftel, P. Kristinsdottir, and E. Johnson (1985), Continuous impurity analysis along the Dye 3 deep core, in *Greenland Ice Core: Geophysics, Geochemistry, and the Environment*, *Geophys. Monogr. Ser.*, vol. 33, edited by C. C. Langway Jr., H. Oeschger and W. Dansgaard, pp. 90–94, AGU, Washington, D. C.

Hewitt, C. D., and J. F. B. Mitchell (1997), Radiative forcing and response of a GCM to ice age boundary conditions: Cloud feedback, and climate sensitivity, *Clim. Dyn.*, *13*(11), 821–834, doi:10.1007/s003820050199.

Howat, I., B. Smith, I. Joughin, and T. Scambos (2008), Rates of southeast Greenland ice volume loss from combined ICESat and ASTER observations, *Geophys. Res. Lett.*, *35*, L17505, doi:10.1029/2008GL034496.

Hutter, K. (1982), A mathematical model of polythermal glaciers and ice sheets, *Geophys. Astrophys. Fluid Dyn.*, *21*, 201–224, doi:10.1080/03091928208209013.

Hutter, K. (1983), *Theoretical glaciology: Material science of ice and the mechanics of glaciers and ice sheets*, D. Reidel, Dordrecht, Netherlands.

Huybrechts, P. (1994), The present evolution of the Greenland ice sheet: An assessment by modelling, *Global Planet. Change*, *9*(1–2), 39–51, doi:10.1016/0921-8181(94)90006-X.

Huybrechts, P. (1996), Basal temperature conditions of the Greenland ice sheet during the glacial cycles, *Ann. Glaciol.*, *23*, 226–236.

Huybrechts, P. (2002), Sea-level changes at the LGM from ice-dynamic reconstructions of the Greenland and Antarctic ice sheets during the glacial cycles, *Quat. Sci. Rev.*, *21*(1–3), 203–231, doi:10.1016/S0277-3791(01)00082-8.

Huybrechts, P., and J. de Wolde (1999), The dynamic response of the Greenland and Antarctic ice sheets to multiple-century climatic warming, *J. Clim.*, *12*(8), 2169–2188, doi:10.1175/1520-0442(1999)012<2169:TDROTG>2.0.CO;2.

Huybrechts, P., and S. T'siobbel (1995), Thermomechanical modelling of northern hemisphere ice sheets with a two-level mass-balance parameterisation, *Ann. Glaciol.*, *21*, 111–116.

Huybrechts, P., O. Rybak, F. Pattyn, U. Ruth, and D. Steinhage (2007), Ice thinning, upstream advection, and non-climatic biases for the upper 89% of the EDML ice core from a nested model of the Antarctic ice sheet, *Clim. Past*, *3*, 577–589, doi:10.5194/cp-3-577-2007.

Imbrie, J. Z., J. D. Hays, D. G. Martinson, A. MacIntyre, A. C. Mix, J. J. Morley, N. G. Pisias, W. L. Prell, and N. J. Shackleton (1984), The orbital theory of Pleistocene climate: Support from a revised chronology of the marine d18O record, in *Milankovitch and Climate: Understanding the Response to Astronomical Forcing. Part* 1, edited by A. Berger et al., pp. 269–305, D. Reidel, Dordrecht, Netherlands.

Johnsen, S. J., D. Dahl-Jensen, W. Dansgaard, and N. S. Gundestrup (1995), Greenland paleotemperatures derived from GRIP borehole temperature and ice core isotope profiles, *Tellus B*, *47*(5), 624–629.

Johnson, J., and J. L. Fastook (2002), Northern Hemisphere glaciation and its sensitivity to basal melt water, *Quat. Int.*, *95–96*, 65–74.

Joughin, I., M. Fahnestrock, S. Ekholm, and R. Kwok (1997), Balance velocities of the Greenland ice sheet, *Geophys. Res. Lett.*, *24*(23), 3045–3048, doi:10.1029/97GL53151.

Jouzel, J., et al. (1993), Extending the Vostok ice-core record of paleoclimate to the penultimate glacial period, *Nature*, *364*, 407–412, doi:10.1038/364407a0.

Jouzel, J., et al. (1997), Validity of the temperature reconstruction from water isotopes in ice cores, *J. Geophys. Res.*, *102*, 26,471–26,487, doi:10.1029/97JC01283.

Kubatzki, C., M. Claussen, R. Calov, and A. Ganopolski (2006), Sensitivity of the Last Glacial Inception to initial and surface conditions, *Clim. Dyn.*, *27*, 333–344, doi:10.1007/s00382-006-0136-6.

Layberry, R. L., and J. L. Bamber (2001), A new ice thickness and bed data set for the Greenland ice sheet 2. Relationship between dynamics and basal topography, *J. Geophys. Res.*, *106*, 33,781–33,788, doi:10.1029/2001JD900053.

Le Meur, E., and P. Huybrechts (1996), A comparison of different ways of dealing with isostasy: Examples from modelling the Antarctic ice sheet during the last glacial cycle, *Ann. Glaciol.*, *23*, 309–317.

Le Meur, E., and P. Huybrechts (2001), A model computation of the temporal changes of surface gravity and geoidal signal induced by the evolving Greenland ice sheet, *Geophys. J. Int.*, *145*, 835–849, doi:10.1046/j.1365-246x.2001.01442.x.

Letreguilly, A., P. Huybrechts, and N. Reeh (1991), Steady state characteristics of the Greenland ice sheet under different climates, *J. Glaciol.*, *37*(125), 149–157.

Marshall, S. J., and K. M. Cuffey (2000), Peregrinations of the Greenland ice sheet divide in the last glacial cycle: Implications for central Greenland ice cores, *Earth Planet. Sci. Lett.*, *179*(1), 73–90, doi:10.1016/S0012-821X(00)00108-4.

Marsiat, I. (1994), Simulation of the Northern Hemisphere continental ice sheets over the last glacial-interglacial cycle: Experiments with a latitude-longitude vertically integrated ice sheet model coupled to a zonally averaged climate model, *Palaeoclimates*, *1*(1), 59–98.

Mayewski, P. A., and M. Bender (1995), The GISP2 ice core record-paleoclimate highlights, *Rev. Geophys.*, *33*(S1), 1287–1296, doi:10.1029/95RG00498.

Meese, D., R. Alley, T. Gow, P. M. Grootes, P. Mayewski, M. Ram, K. Taylor, E. Waddington, and G. Zielinski (1994), Preliminary depth-age scale of the GISP2 ice core, *CRREL Spec. Rep.*, 94-1, U.S. Army Corps of Eng. Cold Reg. Res. and Eng. Lab., Hanover, NH.

Morland, L. W. (1984), Thermomechanical balances of ice sheet flows, *Geophys. Astrophys. Fluid Dyn.*, *29*, 237–266, doi:10.1080/03091928408248191.

Paterson, W. S. B. (1994), *The Physics of Glaciers*, 3rd ed., Elsevier, Oxford, U. K.

Pattyn, F. (1999), The variability of Antarctic ice-sheet response to the climatic signal, *Ann. Glaciol.*, *29*, 273–278, doi:10.3189/172756499781821067.

Pattyn, F. (2006), GRANTISM: An Excel model for Greenland and Antarctic ice sheet response to climate changes, *Comput. Geosci.*, *32*(3), 316–325, doi:10.1016/j.cageo.2005.06.020.

Pattyn, F., and H. Decleir (1998), Ice dynamics near Antarctic marginal mountain ranges: Implications for interpreting the glacial-geological signal, *Ann. Glaciol.*, *27*, 327–332.

Payne, A. J., and D. J. Baldwin (1999), Thermomechanical modelling of the Scandinavian ice sheet: Implications for ice-stream formation, *Ann. Glaciol.*, *28*, 83–89, doi:10.3189/172756499781821733.

Petit, J. R., et al. (1999), Climate and atmospheric history of the past 420,000 years from the Vostok ice core, Antarctica, *Nature*, *399*(6735), 429–436, doi:10.1038/20859.

Pollack, H. N., S. J. Hurter, and J. R. Johnson (1993), Heat flow from the Earth's interior: Analysis of the global data set, *Rev. Geophys.*, *31*(3), 267–280, doi:10.1029/93RG01249.

Reeh, N. (1991), Parameterization of melt rate and surface temperature on the Greenland ice sheet, *Polarforschung*, *59*(3), 113–128.

Ridley, J., P. Huybrechts, J. M. Gregory, and J. Lowe (2005), Elimination of the Greenland ice sheet in a high-CO2 climate, *J. Clim.*, *18*(17), 3409–3427, doi:10.1175/JCLI3482.1.

Ritz, C., A. Fabre, and A. Letreguilly (1997), Sensitivity of a Greenland ice sheet model to ice flow and ablation parameters: Consequences for the evolution through the last climatic cycle, *Clim. Dyn.*, *13*(1), 11–24, doi:10.1007/s003820050149.

Ritz, C., V. Rommelaere, and C. Dumas (2001), Modeling the Antarctic ice sheet evolution of the last 42,0000 years: Implication for altitude changes in the Vostok region, *J. Geophys. Res.*, *106*, 31,943–31,964, doi:10.1029/2001JD900232.

Rückamp, M., N. Blindow, S. Suckro, M. Braun, and A. Humbert (2010), Dynamics of the ice cap on King George Island, Antarctica: Field measurement and numerical simulations, *Ann. Glaciol.*, *51*(55), 80–90, doi:10.3189/172756410791392817.

Rybak, O. O., and P. Huybrechts (2008), Sensitivity of the EDML ice core chronology to the geothermal heat flux, *Mater. Glatsiologicheskikh Issled.*, *105*, 35–40.

Sowers, T., M. Bender, L. Labeyrie, D. Martinson, J. Jouzel, D. Raynaud, J. J. Pichon, and Y. Korotkevich (1993), 135,000 year Vostok-SPECMAP common temporal framework, *Paleoceanography*, *8*, 737–766, doi:10.1029/93PA02328.

Takeda, A. L., S. J. Cox, and A. J. Payne (2002), Parallel numerical modelling of the Antarctic Ice Sheet, *Comput. Geosci.*, *28*, 723–734, doi:10.1016/S0098-3004(01)00106-6.

Tarasov, L., and W. R. Peltier (1999), Impact of thermomechanical ice sheet coupling on a model of the 100 kyr ice age cycle, *J. Geophys. Res.*, *104*, 9517–9545, doi:10.1029/1998JD200120.

Tarasov, L., and W. R. Peltier (2002), Greenland glacial history and local geodynamic consequences, *Geophys. J. Int.*, *150*(1), 198–229, doi:10.1046/j.1365-246X.2002.01702.x.

Tarasov, L., and W. R. Peltier (2003), Greenland glacial history, borehole constraints, and Eemian extent, *J. Geophys. Res.*, *108*(B3), 2143, doi:10.1029/2001JB001731.

Tarasov, L., and W. R. Peltier (2004), A geophysically constrained large ensemble analysis of the deglacial history of the North American ice sheet complex, *Quat. Sci. Rev.*, *23*, 359–388, doi:10.1016/j.quascirev.2003.08.004.

Thomas, R. H., B. M. Csatho, S. Gogineni, K. C. Jezek, and K. Kuivinen (1998), Thickening of the western part of the Greenland ice sheet, *J. Glaciol.*, *44*(148), 653–658.

van de Wal, R. S. W. (1999), Processes of buildup and retreat of the Greenland ice sheet, *J. Geophys. Res.*, *104*, 3899–3906, doi:10.1029/1998JD200030.

Velicogna, I. (2009), Increasing rates of ice mass loss from the Greenland and Antarctic ice sheets revealed by GRACE, *Geophys. Res. Lett.*, *36*, L19503, doi:10.1029/2009GL040222.

Watanabe, O., J. Jouzel, S. Johnsen, F. Parrenin, H. Shoji, and N. Yoshida (2003), Homogeneous climate variability across East Antarctica over the past three glacial cycles, *Nature*, *422*, 509–512, doi:10.1038/nature01525.

Zweck, C., and P. Huybrechts (2003), Modeling the marine extent of northern hemisphere ice sheets during the last glacial cycle, *Ann. Glaciol.*, *37*, 173–180, doi:10.3189/172756403781815870.

K. Fleming, Western Australian Centre for Geodesy, Curtin University of Technology, GPO Box U1987, Perth, WA 6845, Australia. (k.fleming@curtin.edu.au)

J. M. Hagedoorn, I. Rogozhina, and M. Thomas, Helmholtz Centre Potsdam, GFZ German Research Centre for Geosciences, Section 1.3: Earth System Modelling, Telegrafenberg, D-14473 Potsdam, Germany. (jan@gfz-potsdam.de; valmont@gfz-potsdam.de; mthomas@gfz-potsdam.de)

Z. Martinec, Dublin Institute for Advanced Studies, 5 Merrion Square, Dublin 2, Ireland. (zdenek@cp.dias.ie)